Vicarious Calibration of ASTER Thermal Infrared Bands

Hideyuki Tonooka, *Member, IEEE*, Frank D. Palluconi, Simon J. Hook, and Tsuneo Matsunaga

***Abstract*—The Advanced Spaceborne Thermal Emission and Reflection Radiometer (ASTER) on the Terra satellite has five bands in the thermal infrared (TIR) spectral region between 8–12 μm. The TIR bands have been regularly validated in-flight using ground validation targets. Validation results are presented from 79 experiments conducted under clear sky conditions. Validation involved predicting the at-sensor radiance for each band using a radiative transfer model, driven by surface and atmospheric measurements from each experiment, and then comparing the predicted radiance with the ASTER measured radiance. The results indicate the average difference between the predicted and the ASTER measured radiances was no more than 0.5% or 0.4 K in any TIR band, demonstrating that the TIR bands have exceeded the preflight design accuracy of < 1 K for an at-sensor brightness temperature range of 270–340 K. The predicted and the ASTER measured radiances were then used to assess how well the onboard calibration accounted for any changes in both the instrument gain and offset over time. The results indicate that the gain and offset were correctly determined using the onboard blackbody, and indicate a responsivity decline over the first 1400 days of the Terra mission.**

***Index Terms*—Degradation, field experiment, gain, offset, onboard calibration, radiative transfer, responsivity, spectral emissivity, surface temperature, vicarious calibration.**

I. Introduction

THE need for in-flight validation of thermal infrared sensors has been recognized since the launch of the early thermal infrared sensors on the Earth Resources Technology Satellites, later renamed Landsat. In-flight validation or vicarious calibration (VC) is an on-orbit technique in which calibrated ground-based or airborne radiometers deployed on or above a spectrally and spatially homogeneous target take simultaneous measurements during periods of aircraft or satellite instrument overpasses [1]. These measurements may be made on a nearly continuous basis at long-term validation sites or individual campaigns may be conducted for short periods that focus on a particular sensor or group of sensors. This paper provides an assessment of the in-flight validation of the thermal infrared bands on the Advanced Spaceborne Thermal Emission and Reflectance Radiometer (ASTER) [2] using results from field campaigns at the Salton Sea, CA, Railroad Valley and Cold Springs Reservoir, NV, and Lake Kasumigaura, Japan, and results from a long-term validation site at Lake Tahoe CA/NV.

Manuscript received October 29, 2004; revised May 23, 2005. This work was supported in part by the Earth Remote Sensing Data Analysis Center, Tokyo, and the Jet Propulsion Laboratory, California Institute of Technology, Pasadena, under Contract with the National Aeronautics and Space Administration as part of the Earth Observing System Mission to Planet Earth Program.

H. Tonooka is with Ibaraki University, Ibaraki 316-8511, Japan (e-mail: tonooka@mx.ibaraki.ac.jp).

F. D. Palluconi and S. Hook are with the Jet Propulsion Laboratory, California Institute of Technology, Pasadena, CA 91109 USA.

T. Matsunaga is with the National Institute for Environmental Studies, Ibaraki 305-8506, Japan.

Digital Object Identifier 10.1109/TGRS.2005.857885

TABLE I
SUMMARY CHARACTERISTICS OF THE ASTER/TIR INSTRUMENT

Spatial resolution	90 m
Swath width	60 km
Signal quantization levels	12 bits
NEΔT	$\leq$ 0.3 K
Absolute temperature accuracy (design values)	$\leq$ 3 K (200–240 K)
	$\leq$ 2 K (240–270 K)
	$\leq$ 1 K (270–340 K)
	$\leq$ 2 K (340–370 K)
Spectral band passes	Band 10: 8.125–8.475 μm
	Band 11: 8.475–8.825 μm
	Band 12: 8.925–9.275 μm
	Band 13: 10.25–10.95 μm
	Band 14: 10.95–11.65 μm

II. ASTER

The ASTER instrument is a high-spatial resolution 14-band multispectral imager on the Terra satellite. The Terra satellite was launched in December 1999 and is the first satellite in the National Aeronautics and Space Administration's Earth Observing System. The ASTER instrument consists of three subsystems divided by spectral range: the visible and near-infrared (VNIR), the short-wave infrared (SWIR), and the thermal infrared (TIR). The TIR subsystem, discussed in this paper, has five spectral bands (bands 10–14) with a spatial resolution of 90 m. These bands allow the retrieval of both the surface temperature and the surface spectral emissivity, which can be used in a wide variety of studies such as environmental monitoring and hazard prediction. Table I shows the summary characteristics of the ASTER/TIR instrument subsystem.

Each of the three subsystems has an onboard radiometric calibration system for converting the digital numbers (DNs) measured by the subsystem to radiance. Periodic inflight validation experiments (VC) have been conducted to check the accuracy of the calibrated data [3]. This paper summarizes the VC activities related to the TIR subsystem including the results from an assessment of the radiometric performance.

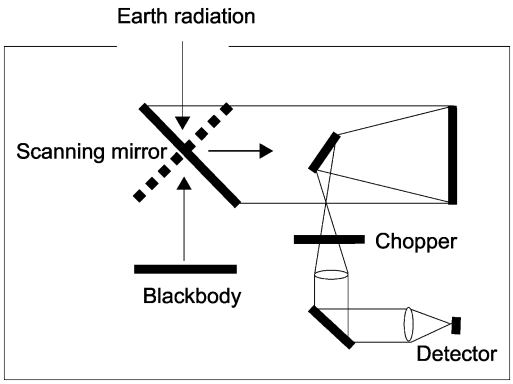

Fig. 1. Optical unit of the ASTER TIR instrument.

III. ASTER/TIR Onboard Calibration

A. Overview

The TIR subsystem obtains images by mechanical scanning with ten mercury–cadmium–telluride photoconductive detectors which are aligned along the track for each band (50 detectors in total) and cooled to 80 K using a mechanical split Stirling cycle cooler [4]. The gain of the TIR subsystem is fixed unlike the gain of the VNIR and SWIR subsystems. Uncalibrated DNs observed by each of the TIR detectors are converted to calibrated radiance (R) using the quadratic formula

$$R = C_0 + C_1 \times \mathrm{DN} + C_2 \times \mathrm{DN}^2 \tag{1}$$

where C_0, C_1, and C_2 are radiometric calibration coefficients (RCCs). The C_2 coefficient is fixed preflight and the C_0 and C_1 coefficients are updated inflight. These coefficients vary depending on the optics and electronics and each detector has a different set of RCCs. The coefficients are obtained using data from the onboard blackbody. The onboard blackbody is a full-aperture honeycombed blackbody with an emissivity greater than 0.99 that can be heated between 270–340 K [5]. The blackbody is measured by rotation of a scanning mirror, as shown in Fig. 1.

In order to obtain the offset coefficient in (1) (C_0) the blackbody is set to a particular temperature (270 K) and imaged prior to each Earth observation. In other thermal infrared systems this data point would typically be used with a measurement of deep space to perform a two-point calibration and obtain the gain coefficient C_1 (the nonlinear coefficient C_2 is typically ignored or fixed to a constant value). However, the ASTER TIR subsystem cannot view deep space, and therefore these data are obtained by periodically heating the blackbody to a series of set point temperatures and imaging the blackbody at each temperature. Four set point temperatures are used which are 270, 300, 320, and 340 K. The imaging of the blackbody prior to each Earth observation is referred to as the short-term calibration (STC), and the periodic imaging of the blackbody at a series of set point temperatures is referred to as the long-term calibration (LTC). In the early part of the mission, LTCs were executed every 17 days, then in April 2001 this interval was increased to every 33 days in order to satisfy a requirement to minimize the number of pointings of the SWIR subsystem.

The C_2 coefficients have been kept to preflight values, though they can also be determined simultaneously with C_1 using an LTC dataset. This is because the C_2 coefficients are sensitive to measurements at 340 K which are less accurate in orbit than measurements at 270, 300, and 320 K.

B. RCCs Applied to Level-1 Processing

In each LTC, the optimum coefficients for C_1 are calculated using a least squares method with the blackbody measurements from the four temperature points. However, the RCCs, which are used for level-1 processing [6], are obtained from the RCC online database which is only updated if a calibration error caused from using old RCCs has exceeded 0.5 K at 300 or 320 K, or 1 K at 340 K. Therefore, the C_1 coefficients from each LTC are not always used with the level-1 processing, while the C_0 coefficients obtained before every Earth observation are always used. In addition, the database has not always been updated in a timely manner due to delays in the analysis and validation of the coefficients derived from the LTC [7]. In particular, the RCCs for database versions 2.05 and 2.06 (see Table V) were not updated in time, which resulted in an error in the reported radiances (for example, a reported error at 320 K in band 12 was reached to -3 K around the end of v2.06 [7]). The RCCs determined since v2.06 have been updated before the error has reached the specified limit (0.5 K at 300 K or 320 K and 1 K at 340 K). In order to correct these errors a user-based recalibration method for level-1 products has been developed [7], [8], and the necessary coefficients to apply this correction for a given scene can be obtained at http://www.science.aster.ersdac.or.jp/RECAL/.

The RCCs for database versions 3.00 or later will be determined by regression equations for each image acquisition date, so that the recalibration will not be necessary for these RCCs.

IV. Vicarious Calibration for TIR Sensors

Ground-based VC can be performed in the TIR spectral region using either a temperature-based approach or a radiance-based approach [3]. Both approaches are described below together with the requirements and limitations of each approach.

A. Theoretical Basis

1) Temperature-Based Method: The temperature-based method is a technique for predicting at-sensor radiance with surface kinetic temperatures measured at a site.

The radiance observed by band k is written by

$$R_k = \int_0^\infty \phi_{k,\lambda} \left[\tau_\lambda \left(\epsilon_\lambda B_\lambda(T_0) + \frac{(1-\epsilon_\lambda) F_\lambda^\downarrow}{\pi} \right) + R_\lambda^\uparrow \right] d\lambda \tag{2}$$

where

λ	wavelength;
$\phi_{k,\lambda}$	normalized spectral response function of band k;
$\epsilon_{0,\lambda}$	surface emissivity;
T_0	surface kinetic temperature;
τ_λ	atmospheric transmittance;
$R_\lambda^\uparrow$	path radiance;
$F_\lambda^\downarrow$	atmospheric downwelling irradiance at the surface;
$B_\lambda(*)$	Planck function.

In the temperature-based method, R_k is derived from (2) with the surface parameters (T_0 and $\epsilon_{0,\lambda}$) measured, and the

atmospheric parameters (τ_λ, $R_\lambda^\uparrow$, and $F_\lambda^\downarrow$) calculated from atmospheric profiles by using a radiation transfer code such as MODTRAN [9]. In the radiative transfer calculation, air-temperature and humidity profiles are key parameters, which are typically measured by a radiosonde launched from the site, or provided from other sources such as a numerical forecast model if radiosonde data are not available.

If the spectral variation in emissivity of the material is small, e.g., water, and the bandwidth of the sensor is sufficiently narrow, (2) can be rewritten as

$$R_k = \tau_k \left(\epsilon_k B_k(T_0) + \frac{(1-\epsilon_{0,k})F_k^\downarrow}{\pi} \right) + R_k^\uparrow \tag{3}$$

where each parameter with the subscript k is expressed by

$$x_k = \int_0^\infty \phi_{k,\lambda} x_\lambda d\lambda. \tag{4}$$

A theoretical simulation study for the ASTER/TIR bands indicated the error using (3) was at most 0.03% in any of the bands for a water surface with a constant temperature in the temperature range 0 °C to 60 °C. The simulation study used the MODTRAN radiative transfer model to simulate the atmospheric effects with the 1976 U.S. Standard model atmosphere [9]. Using the emissivity for a soil sample taken from the Railroad Valley site (sample no. 88P4699 in [10]), the error increased slightly but was 0.2% at most (< 0.1 K in temperature).

2) Radiance-Based Method: Equation (3) is rewritten by

$$R_k = \tau_k R_{0,k} + R_k^\uparrow \tag{5}$$

where $R_{0,k}$ is the at-surface radiance defined by

$$R_{0,k} = \epsilon_k B_k(T_0) + \frac{(1-\epsilon_{0,k})F_k^\downarrow}{\pi}. \tag{6}$$

In the radiance-based method, R_k is calculated from (5) with the at-surface radiance measured directly and the atmospheric parameters (τ_λ and $R_\lambda^\uparrow$) calculated from atmospheric profiles using a radiative transfer code. That is, the radiance-based method does not need field measurements of surface temperature and emissivity which are necessary in the temperature-based method. If an airborne radiometer is available, only the atmospheric effects between the plane and space need to be considered when calculating τ_k and $R_k^\uparrow$. This method is simpler than the temperature-based method and is also free from a complicated measurement of spectral emissivity, but the spectral response functions of the *in situ* radiometer and target sensor need to match otherwise the temperature-based method should be utilized.

B. Conditions Required for VC Sites

Certain site conditions are required for validation of TIR data [1], [11].

1) Surface Conditions: The sites should be homogenous in both surface temperature and emissivity. For land sites a nearly shadow free surface aids in minimizing temperature contrast across the surface. Sites which typically meet these criteria include water bodies, dry lake beds, and snow-covered areas. Some of such sites may not be suitable for validation of reflectance data since the spectral features observed in the TIR may differ from those observed in the solar reflected region. Vegetated surfaces are not appropriate, since the observed brightness temperature can be a strong function of the viewing angle and position. If a water site is used the surface emissivity from a spectral library [10], [12] can be assumed, and an *in situ* measurement of emissivity is not required. If a land site is used, such as a dry lake bed (Playa), the emissivity needs to be determined from either *in situ* emissivity measurements or the laboratory emissivity measurement of field samples. The temperature range that can be validated at a site depends on the type of site. For example, snow/ice-covered areas can be used to validate temperatures around 0 °C or lower. Water sites can be used to validate temperatures between 0 °C and 30 °C, roughly, and dry lake beds in deserts can be used to validate a wide range of temperatures with maximum temperatures in excess of 50 °C. A combination of sites is desirable to provide measurements across a wide radiance range.

2) Atmospheric Conditions: Stable cloud-free conditions are ideal. In addition, the total water vapor amount in the atmosphere above the site should be small (ideally $\leq$ 1 cm in our experience), since the accuracy of the radiative transfer calculation is directly related to the knowledge of the water vapor above the site. As a result high-elevation or arid sites are generally used for VC.

3) Accessibility: The site should be easily accessible by investigators. This is not scientifically important but is practically important, especially if a large number of ground validation campaigns are planned at the site.

V. VC Sites for ASTER/TIR Bands

A. Overview

VC experiments for the TIR subsystem have been regularly conducted by the authors since March 12, 2000. Table II lists 79 experiments conducted under clear sky conditions from March 2000 to February 2004, including the date of the experiment, site name, site type (water or land), mean brightness temperature observed by ASTER, VC method (temperature-based or radiance-based), RCC verified by trend analysis (described later), and investigator. In some cases, the investigators conducted largely independent validation experiments on the same day where atmospheric data were shared but not surface measurements. Although the forward calculation of the predicted radiance at sensor was calculated using the same radiative transfer model, the model code was independently implemented and operated at the different research institutes represented by the investigators.

B. Lake Tahoe

Lake Tahoe is located at 39° N, 120° W in the Sierra Nevada Mountains. The lake, which is the largest Alpine lake in North America, straddles the border between California and Nevada. Lake Tahoe is the 11th deepest lake in the world with a maximum depth of about 500 m. This site is high (2 km), and atmosphere above the site is typically dry with low total column

TABLE II
SEVENTY-NINE VC EXPERIMENTS FOR ASTER/TIR CONDUCTED UNDER CLEAR SKY CONDITIONS FROM MARCH 2000 TO FEBRUARY 2004. BT: THE MEAN BRIGHTNESS TEMPERATURE OBSERVED BY ASTER (IN DEGREES CELSIUS). METHOD: TEMPERATURE-BASED (TMP) OR RADIANCE-BASED (RAD). RCC: RCC VERIFIED BY TREND ANALYSIS. SITE NAMES ARE LT: LAKE TAHOE, SS: SALTON SEA, LK: LAKE KASUMIGAURA, CSR: COLD SPRINGS RESERVOIR, RRP: RAILROAD PLAYA, AND LL: LUNAR LAKE

No.	Date	Site	Type	BT	Method	RCC	Investigator	No.	Date	Site	Type	BT	Method	RCC	Investigator
1	2000/3/12	LT	Water	3.8	TMP	C_0	Hook	41	2002/2/6	LT	Water	3	TMP	C_0	Hook
2	2000/3/12	LT	Water	3.1	TMP	C_0	Palluconi	42	2002/2/15	LK	Water	3.2	TMP	C_0	Tonooka
3	2000/3/12	LT	Water	3.6	TMP	C_0	Tonooka	43	2002/3/19	LK	Water	8.9	TMP	C_1	Tonooka
4	2000/5/16	LK	Water	16.7	TMP	C_1	Tonooka	44	2002/6/6	LT	Water	14	TMP	C_1	Hook
5	2000/6/4	SS	Land	45.6	RAD	C_1	Matsunaga	45	2002/6/7	LT	Water	10.5	TMP	C_1	Hook
6	2000/6/4	SS	Water	25.8	TMP	C_1	Palluconi	46	2002/6/17	CSR	Water	22.2	TMP	—	Palluconi
7	2000/6/4	SS	Water	25.8	TMP	C_1	Tonooka	47	2002/6/17	CSR	Water	21.6	TMP	—	Tonooka
8	2000/6/11	CSR	Water	18.1	TMP	—	Tonooka	48	2002/6/17	RRP	Land	43.2	RAD	C_1	Matsunaga
9	2000/6/11	RRP	Land	39.6	RAD	C_1	Matsunaga	49	2002/6/17	RRP	Land	43.5	TMP	C_1	Palluconi
10	2000/6/24	LT	Water	11.9	TMP	C_1	Hook	50	2002/6/22	LT	Water	11.8	TMP	C_1	Hook
11	2000/8/4	LT	Water	14.7	TMP	C_1	Hook	51	2002/8/13	SS	Water	28.2	TMP	C_1	Palluconi
12	2000/8/7	SS	Water	26.3	TMP	C_1	Palluconi	52	2002/8/20	RRP	Land	34.8	TMP	C_1	Palluconi
13	2000/8/19	LT	Water	15.7	TMP	C_1	Hook	53	2002/9/2	LT	Water	14.6	TMP	C_1	Hook
14	2000/11/7	LT	Water	8.1	TMP	C_1	Hook	54	2002/9/10	LT	Water	14.8	TMP	C_1	Hook
15	2000/11/7	LT	Water	8	TMP	C_1	Palluconi	55	2002/9/26	LT	Water	14	TMP	C_1	Hook
16	2000/11/7	LT	Water	8	TMP	C_1	Tonooka	56	2002/10/12	LT	Water	11.8	TMP	C_1	Hook
17	2001/2/27	LT	Water	3.1	TMP	C_0	Hook	57	2002/11/4	LT	Water	9.6	TMP	C_1	Hook
18	2001/2/28	LT	Water	2.5	TMP	C_0	Hook	58	2002/11/29	LT	Water	6.3	TMP	C_0	Hook
19	2001/3/2	LT	Water	2.7	TMP	C_0	Palluconi	59	2002/11/30	LT	Water	6.1	TMP	C_0	Hook
20	2001/3/16	LK	Water	6.1	TMP	C_0	Tonooka	60	2002/12/3	SS	Land	19.5	RAD	C_1	Matsunaga
21	2001/3/16	LT	Water	2.2	TMP	C_0	Hook	61	2002/12/3	SS	Water	14.7	TMP	C_1	Palluconi
22	2001/6/3	LT	Water	9.3	TMP	C_1	Hook	62	2002/12/3	SS	Water	14.7	TMP	C_1	Tonooka
23	2001/6/7	SS	Land	41.1	RAD	C_1	Matsunaga	63	2003/6/29	SS	Land	42.7	RAD	C_1	Matsunaga
24	2001/6/7	SS	Water	25	TMP	C_1	Palluconi	64	2003/6/29	SS	Water	26.3	TMP	C_1	Palluconi
25	2001/6/7	SS	Water	25	TMP	C_1	Tonooka	65	2003/6/29	SS	Water	26.3	TMP	C_1	Tonooka
26	2001/6/14	CSR	Water	16.9	TMP	—	Palluconi	66	2003/7/6	LL	Land	39.2	RAD	C_1	Tonooka
27	2001/6/14	CSR	Water	16.7	TMP	—	Tonooka	67	2003/7/6	RRP	Land	43.1	RAD	C_1	Matsunaga
28	2001/6/14	RRP	Land	39.7	RAD	C_1	Matsunaga	68	2003/7/11	LT	Water	17.3	TMP	C_1	Hook
29	2001/6/14	RRP	Land	38.4	TMP	C_1	Palluconi	69	2003/7/12	LT	Water	15	TMP	C_1	Hook
30	2001/7/22	LT	Water	12.5	TMP	C_1	Hook	70	2003/7/22	RRP	Land	43.5	TMP	C_1	Palluconi
31	2001/8/17	RRP	Land	41.7	TMP	C_1	Palluconi	71	2003/8/12	LT	Water	16.3	TMP	C_1	Hook
32	2001/8/22	LT	Water	14.7	TMP	C_1	Hook	72	2003/8/29	LT	Water	16.2	TMP	C_1	Hook
33	2001/9/27	SS	Water	26.1	TMP	C_1	Palluconi	73	2003/9/21	LT	Water	14.1	TMP	C_1	Hook
34	2001/10/9	LT	Water	13	TMP	C_1	Hook	74	2003/9/30	LT	Water	13.8	TMP	C_1	Hook
35	2001/11/3	LT	Water	10.3	TMP	C_1	Hook	75	2003/10/8	LT	Water	13.4	TMP	C_1	Hook
36	2002/1/13	LT	Water	3.8	TMP	C_0	Hook	76	2004/1/20	LK	Water	2.2	TMP	C_0	Tonooka
37	2002/1/14	LT	Water	3.6	TMP	C_0	Hook	77	2004/2/5	LK	Water	2.8	TMP	C_0	Tonooka
38	2002/1/17	SS	Land	17.8	RAD	C_1	Matsunaga	78	2004/2/11	LT	Water	3.2	TMP	C_0	Hook
39	2002/1/17	SS	Water	11.5	TMP	C_1	Palluconi	79	2004/2/12	LT	Water	3.3	TMP	C_0	Hook
40	2002/1/17	SS	Water	11.6	TMP	C_1	Tonooka								

amounts of atmospheric water vapor (0.5–1.5 cm). The lake does not freeze in the winter due to its extreme depth and can be used for validation throughout the year. The probability of cloud-free conditions is high, except in the winter months. The Jet Propulsion Laboratory (JPL) has deployed four permanently moored buoys at the site (Fig. 2). Each buoy makes a variety of temperature and meteorological measurements including the bulk temperature and surface skin temperature on a nearly continuous basis (every 2 min). The surface skin temperature is measured using radiometers developed by JPL which have an accuracy of better than 0.1 K that has been confirmed in both sea trials and laboratory comparisons [13].

C. Salton Sea

Salton Sea is located in southeast California and has the largest areal extent of all the California lakes. The sea has a maximum depth of ~ 16 m and surface elevation of ~ 70 m below sea level. The total column water above the site is quite variable and can exceed 4 cm. However, the atmosphere can be fairly dry, and due to the lake's location and shallow depth,

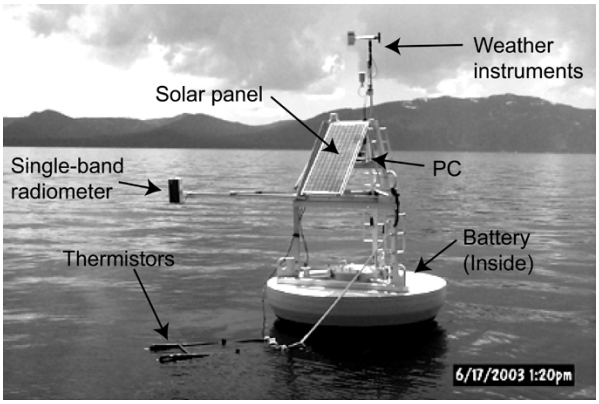

Fig. 2. One of the four permanently moored buoys on Lake Tahoe. Radiometers, bulk temperature measuring sensors, weather instruments, and wireless communication are equipped.

the water temperatures frequently exceed 30 °C in the summer, allowing validation at very high temperatures for a water site.

D. Railroad Valley

Railroad Valley is located in south-central Nevada. The weather is usually clear and stable in the summer. There are two validation sites located in Railroad Valley: the Railroad Playa and the Lunar Lake Playa. These sites are frequently used for VC of sensors which measure solar reflected radiation [14], [15]. The Railroad Playa is a large dry lake that is about 17 km long and 13 km wide and has an elevation of 1470 m above sea level. Lunar Lake, also a dry lake, is located about 25 km west of Railroad Playa. Lunar Lake is considerably smaller than Railroad Playa ($4\times$ 2 km) and therefore cannot be used to validate sensors with large multikilometer footprints. However, the playa surface is far more homogenous than the Railroad Playa surface and as a result is a better target for validation of small footprint sensors such as Landsat and ASTER. The playa surface is 1750 m above sea level.

E. Cold Springs Reservoir

Cold Springs Reservoir (CSR) is a small artificial reservoir located in White River Valley, next to Railroad Valley. The reservoir is about 1.6 km long, 400–800 m wide, and 0.5–5 m deep. The surface elevation is 1560 m above sea level. The predicted radiances were not in good agreement with the ASTER instrument radiances in the initial validation experiments. This discrepancy was found to be caused by straylight in the ASTER/TIR instrument [16] and is further described in Section VI-C.

F. Lake Kasumigaura

Lake Kasumigaura is located about 50 km northeast of Tokyo and is the second largest lake in Japan. The lake has an area of 168 km^2 with a maximum depth of about 8 m, and the water level is at sea level. This site is not appropriate for VC in summer due to hot humid conditions, but is available in winter because the air is typically cool, dry, and stable. The typical column water vapor amount is about 0.5 cm in winter compared to about 5–6 cm in summer [17]. Thus, this site was only used in winter.

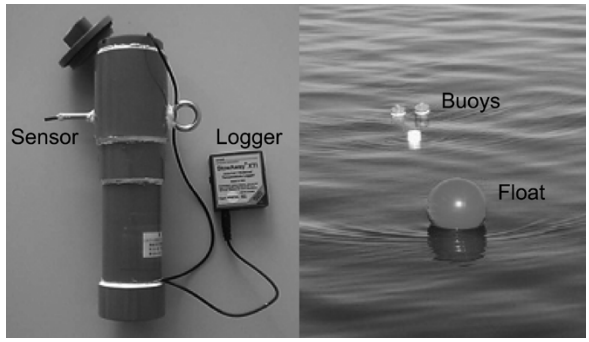

Fig. 3. (Left) Temperature measuring buoy and (right) *in situ* bulk temperature measurement at the Salton Sea on December 3, 2002.

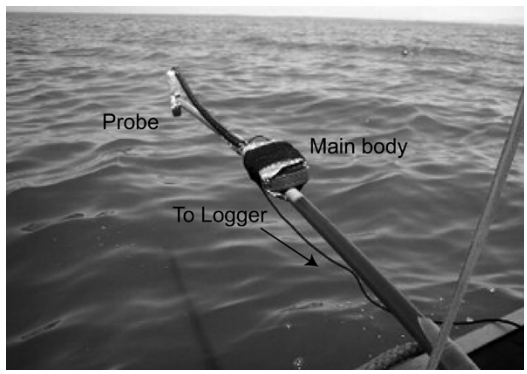

Fig. 4. *In situ* radiometer measurement at Salton Sea on June 29, 2003.

VI. Validation Campaigns and Data Processing

A. Validation Campaigns at the Water Sites

Water is used as a target because it is uniform in composition, has a high and known emissivity, and often exhibits low surface temperature variation (≤ 1 °C) over large areas [18]. At the validation campaign sites (Salton Sea, Cold Springs Reservoir, and Lake Kasumigaura) an estimate of the bulk water temperature was obtained from multiple (5–9) temperature measuring buoys dispersed over an area covering 3×3 the area of an ASTER pixel (270×270 m). The buoys measure and log the bulk water temperature with a thermistor at about 2–4 cm beneath the water surface. Fig. 3 shows a picture of one of the buoys (left) and also a view of the *in situ* bulk temperature measurements made at Salton Sea on December 3, 2002 (right). The bulk water temperature is not the radiating, kinetic, or skin temperature of the water surface which is measured by ASTER. To determine the difference between the bulk water temperature and the water surface radiating temperature, the brightness temperature of the water surface is simultaneously measured with a well-calibrated radiometer deployed near one of the buoys. Fig. 4 shows a picture of an *in situ* radiometer measurement at Salton Sea on June 29, 2003, and Fig. 5 shows plots of the skin and bulk temperatures measured during the same experiment. In order to ensure the radiometer was accurately calibrated, a highly accurate field portable blackbody was measured before and after the satellite overpass [19] together with the surface temperature. The skin temperatures shown were derived from radiometer measurements by calibration with a blackbody, and correcting for the water emissivity and atmospheric downwelling irradiance,

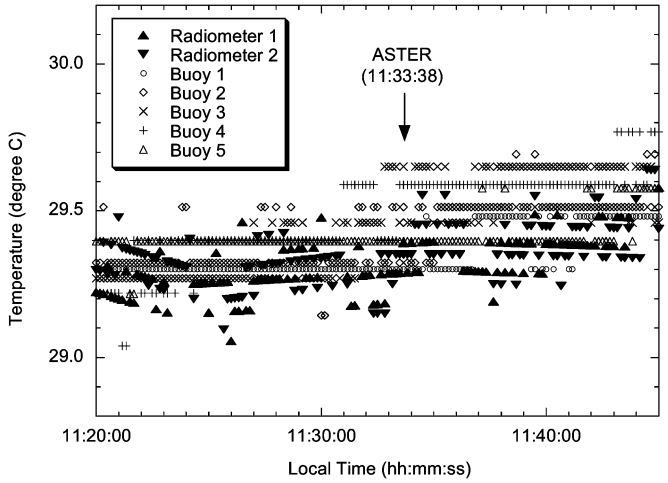

Fig. 5. Plots of the skin and bulk water temperatures measured at Salton Sea on June 29, 2003. The solid triangle points (up and down) show skin temperatures derived from the calibrated radiometer measurements and correction of water emissivity and atmospheric downwelling irradiance. The other points show the bulk temperatures measured by the buoys.

as described later. In addition to the *in situ* temperature measurements, multiple atmospheric sounding balloons were launched at the satellite overpass time to provide an estimate of air temperature and relative humidity. Ground sun photometer measurements were also made to provide a measure of changes in atmospheric opacity and total column water vapor. A meteorological station was also deployed on a boat or on shore that provides measurements of wind velocity, air temperature, and relative humidity. If a radiosonde was not launched, atmospheric profiles near the overpass time acquired from the nearest permanent weather station, or produced from Global Data Assimilation System of National Centers for Environmental Prediction (NCEP) [20], were used. The *in situ* temperatures measured by the calibrated radiometers were converted to skin temperatures by

$$T_s = B_k^{-1}\left(\frac{B_k(T_b) - \frac{(1-\epsilon_{k,w})F_k^{\downarrow}}{\pi}}{\epsilon_{k,w}}\right) \tag{7}$$

where

T_s skin temperature;
T_b calibrated brightness temperature;
$\epsilon_{k,w}$ water emissivity, weighted with the response function of the radiometer $\phi_k(\lambda)$;
$F_k^{\downarrow}$ atmospheric downwelling irradiance at the surface, computed by MODTRAN and then weighted with $\phi_k(\lambda)$;
$B_k^{-1}(*)$ inverse Planck function.

In this equation the bulk water to skin temperature difference is determined for the buoy nearest the radiometer, and this difference is applied across the array of buoys. This difference has always been between ± 1 °C. With the time of image acquisition known, the mean skin temperature is computed from the buoys in the array. Inserting the mean skin temperature, water emissivity for each band, and atmospheric parameters computed by MODTRAN to (3), the at-sensor radiances are derived for the ASTER bands.

TABLE III
COMPARISON OF THE SPECTRAL BAND PASSES (MICRONS) FOR THE ASTER/TIR INSTRUMENT AND THE MULTIBAND FIELD RADIOMETER (CIMEL CE312)

ASTER TIR		CIMEL CE312	
Band 10:	8.125—8.475	Ch. 6:	8.24—8.61
Band 11:	8.475—8.825	Ch. 5:	8.49—8.86
Band 12:	8.925—9.275	Ch. 4:	8.95—9.34
Band 13:	10.25—10.95	Ch. 3:	10.16—10.94
Band 14:	10.95—11.65	Ch. 2:	10.94—11.73

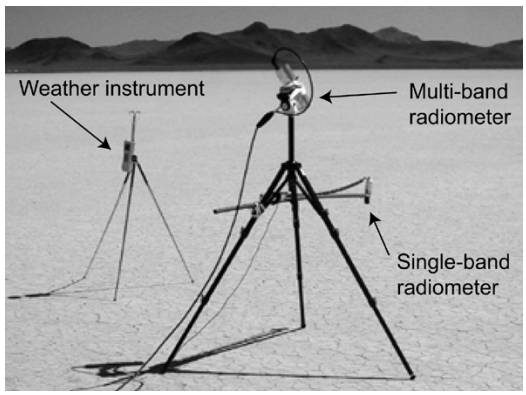

Fig. 6. Surface brightness temperature measurement with the multiband radiometer at Lunar Lake on July 6, 2003 (middle upper). A single-band radiometer (middle lower) and a weather instrument (left) are also shown.

A similar approach was used at the Lake Tahoe site, except that there are four permanently moored buoys and each buoy has a radiometer and several temperature sensors at at depth of 2–3 cm [21], [22]. In some cases, radiometer data were not available at any buoy for a given overpass or for a particular buoy on a given overpass. If no skin temperatures were available for any buoys for a given overpass, the average skin effect (bulk minus skin temperature) for all overpasses was subtracted from the average bulk temperature at each buoy to obtain the station skin temperature. If skin temperatures were available at some buoys, but not all buoys for a given overpass, then the average skin effect (bulk minus skin temperature) for that overpass was calculated and subtracted from the bulk temperatures to obtain the skin temperatures for the buoys without a working radiometer. In the majority of cases atmospheric profiles were obtained from the NCEP. Further details on the atmospheric correction and extraction of the skin temperature from the radiometer data are available in [21] and [22].

B. Field Experiments on Land Sites

For the land sites, the temperature-based method or the radiance-based method was utilized. In some experiments, one or more single-channel radiometers were used with the temperature-based method. The brightness temperatures measured by radiometers were calibrated using blackbody measurements, and then converted to surface kinetic temperatures. In order to convert to surface kinetic temperature, the surface emissivity needs to be known. The surface emissivity was determined at the site using a Fourier transform spectrometer (FTS) [23]. The surface emissivity for each ASTER band was then obtained by

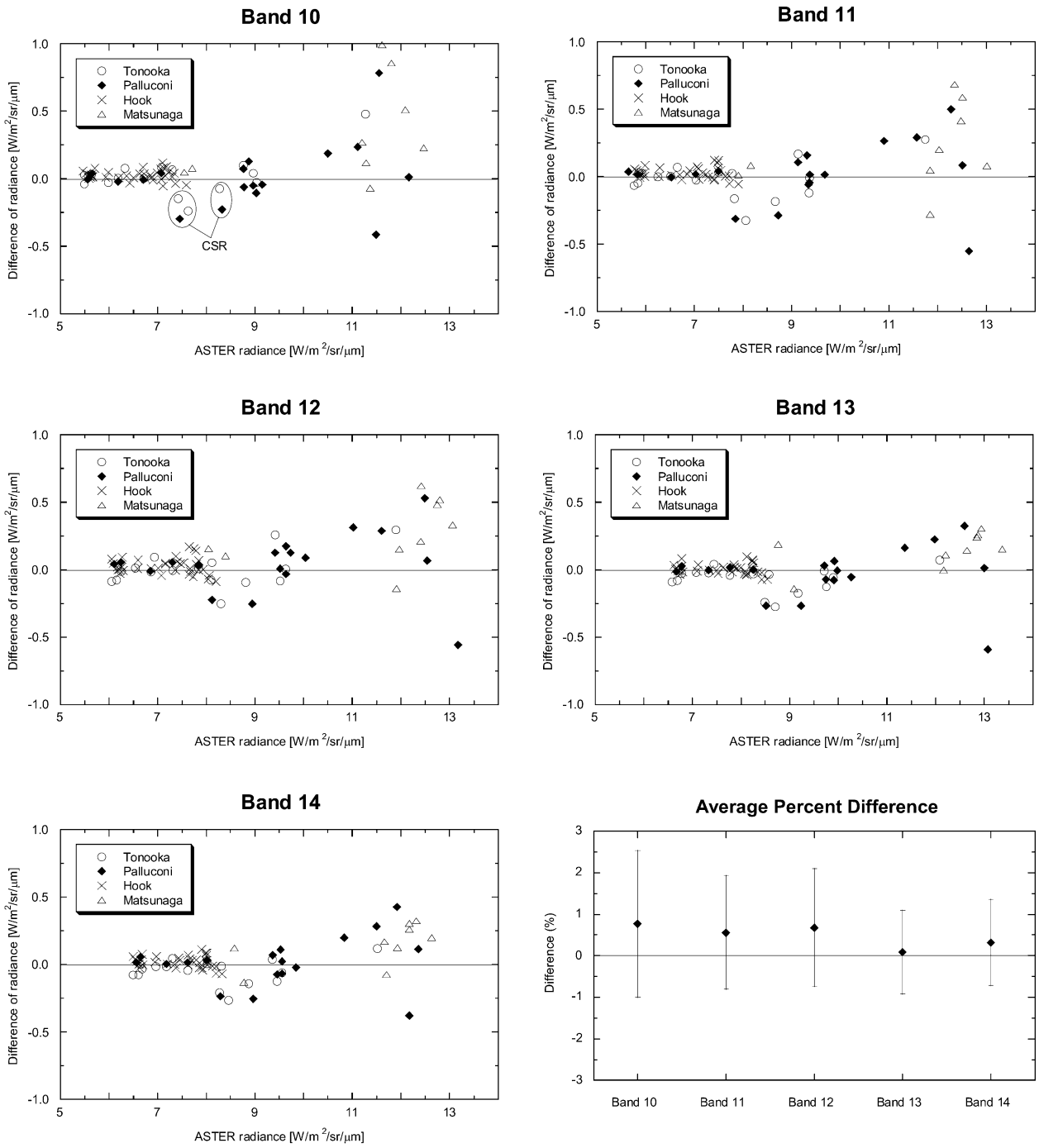

Fig. 7. Plots of the ASTER radiance versus the difference of the VC-based radiance to the ASTER radiance for five bands for 79 VC experiments listed in Table II, shown separately by investigators. For each band, the average percent difference (VC minus ASTER) is also shown with a standard deviation bar at the bottom right.

convolving the system response function of the band with the higher spectral resolution surface emissivity measurement made by the FTS.

In other experiments, multiband radiometers were used with the radiance-based method. These internally calibrated radiometers have five channels that match the five ASTER bands. Table III gives a comparison of the spectral band passes for the ASTER/TIR instrument and the multiband radiometer (CIMEL CE312). The surface brightness temperatures measured with these radiometers were used with (5) to predict the at-sensor radiances. The atmospheric parameters (τ_k and $R_k^{\uparrow}$) in this equation were obtained in the same manner as in the temperature-based method.

Fig. 6 shows a picture of surface brightness temperature measurement with the multiband radiometer at Lunar Lake on July 6, 2003.

C. Comparison With ASTER Radiance

After using the above procedures, the predicted at-sensor radiance and the ASTER at-sensor radiance obtained using the on-

TABLE IV
AVERAGE AND STANDARD DEVIATION OF THE DIFFERENCE BETWEEN THE VC AND ASTER BRIGHTNESS TEMPERATURES AT EACH BAND FOR EACH OF NINE SUBSETS. ON THE RIGHT OF THE AVERAGE, THE STANDARD DEVIATION IS SHOWN IN PARENTHESES. LT: LAKE TAHOE, SS: SALTON SEA, LK: LAKE KASUMIGAURA, CSR: COLD SPRINGS RESERVOIR, RRP: RAILROAD PLAYA, AND LL: LUNAR LAKE

Dataset	Num. of data	Band 10	Band 11	Band 12	Band 13	Band 14
Water and Land Sites						
All	79	0.3 (1.0)	0.2 (0.9)	0.3 (0.9)	−0.1 (0.8)	0.1 (0.9)
All−CSR	74	0.4 (1.0)	0.3 (0.8)	0.4 (0.8)	0.1 (0.7)	0.2 (0.8)
All−9 data*	70	0.2 (0.5)	0.2 (0.5)	0.3 (0.6)	0.0 (0.5)	0.1 (0.6)
Water Sites						
LT	40	0.2 (0.3)	0.2 (0.3)	0.2 (0.4)	0.0 (0.3)	0.1 (0.3)
SS/water	13	0.1 (0.4)	0.1 (0.5)	0.3 (0.5)	−0.2 (0.4)	−0.1 (0.5)
LK	6	0.1 (0.3)	0.0 (0.4)	0.0 (0.5)	−0.3 (0.4)	−0.2 (0.4)
CSR	5	−1.2 (0.6)	−1.6 (0.5)	−1.2 (0.6)	−1.8 (0.3)	−1.7 (0.4)
Land Sites						
RRP & LL	10	1.3 (1.8)	0.8 (1.6)	1.0 (1.7)	0.5 (1.5)	0.9 (1.4)
SS/land	5	1.4 (1.8)	1.0 (1.3)	1.3 (0.7)	0.7 (1.0)	0.8 (1.1)

* 9 data: 4 CSR data, 4 RRP data, and one SS/land data.

board calibrator (OBC) [6] were compared, and used for trend analysis. The ASTER data were geolocated and the location of the site in the image was identified using GPS measurements from the site. The average value of ASTER radiance for a target area was then extracted for each ASTER band. The size of area used for comparison depended on the characteristics of the site, but in general a 2–4 pixel square (180–360 m^2) was used.

Fig. 7 shows plots of the ASTER radiance versus the difference of the VC-based radiance to the ASTER radiance for five bands for the 79 VC experiments listed in Table II, shown separately by investigators, and also the average percent difference (VC minus ASTER) with a standard deviation bar for each band. As shown, the ASTER radiance and the VC-based radiance agree within a few tenths of a percent on average, while the individual band plots indicate some discrepancy for high radiances (> 10 W/m^2/sr/μm for band 10) which were obtained from land sites. The discrepancy in land sites will be discussed later. In the percent difference, bands 10–12 have a slightly larger average bias and variation than bands 13 and 14. A likely explanation for this is most of the land sites are covered by silica-rich materials or clay which show a large variation in emissivity in the wavelength region covered by bands 10–12.

Table IV shows the average and the standard deviation (σ) of the difference between the VC and ASTER brightness- temperatures in each band for each of nine subsets, which indicates the following points. First, the average difference for nearly all datasets is within ± 0.4 K for all bands. This result is far better than the accuracy requirement for this temperature range (≤ 1 K for 270–340 K). The five VCs at CSR indicate a different trend from the other water sites, while giving no impact to the average difference over all dataset. If the nine VCs with largest biases are excluded, the σ over all dataset is reduced to a half. The VCs at the land sites have a larger bias and σ than those at the water sites.

One possible cause for the larger bias and standard deviation of the land sites is the delay in RCC updating, which will cause the ASTER radiance to have a negative bias, and such bias will appear more significantly for higher temperature targets. Thus, the VCs at the land sites have a positive bias (VC $\geq$ ASTER). Another possible cause is difficulty in land surface characterization. Many of our land sites are dry lakes which are much more uniform than typical land surfaces, but are usually less uniform than water sites. Thus, a scale difference between ground measurements and ASTER observation (90 m) will cause a larger error in surface characterization for land sites than for water sites, resulting in a larger σ.

In the water sites except for CSR, the bias is within ± 0.3 K and the σ is less than 0.5 K. The larger bias and standard deviation for CSR is due to straylight effects [16].

The purpose of vicarious calibration is to provide a check on the operation of the OBC and on overall system performance. Over the first 1400 days of operation, the average difference between the VC and ASTER image radiance is no more than 0.5% or 0.4 K in any TIR band. This indicates the instrument is performing well, demonstrating the obtainable accuracy using vicarious methods. The positive average difference seen in most cases is at least in part the result of the periodic updates of the RCCs with a system in which the responsivity is monotonically declining (see Section VII).

VII. TREND ANALYSIS

A. Overview

The RCCs used to correct the ASTER instrument data to radiance are updated periodically in order to account for changes in the TIR subsystem. Since these updates are not done continually, a calibration error, dependent on the time of the acquisition relative to the last RCC update, is introduced [7]. Since the size of the error depends on the target temperature, there will be a different error for sites with different predicted temperatures, even if the ASTER acquisitions were made at exactly the same time. The size of the calibration error is predicted from (1). Because the size of the error induced by the delay in updating the

TABLE V
LIST OF THE RCC VERSION, THE LTC DATE (THE DATE OF THE LTC THAT EACH VERSION WAS MEASURED), THE APPLIED DATE (THE FIRST DATE THAT EACH VERSION WAS APPLIED TO LEVEL-1 PROCESSING), AND THE MEAN OF C_1 OVER DETECTORS

Version	LTC date	Applied date	$C_1 \times 10^3$				
			B10	B11	B12	B13	B14
1.01,02	00/3/12	00/10/15	7.72	7.36	7.14	6.24	5.77
2.03,04	00/9/13	00/9/14	7.80	7.51	7.38	6.27	5.79
2.05	01/1/27	01/2/14	7.87	7.65	7.62	6.38	5.91
2.06	01/8/16	01/12/1	7.99	7.86	7.94	6.55	6.11
2.09	02/5/7	02/10/12	8.14	8.13	8.40	6.79	6.38
2.10	02/8/13	02/11/1	8.16	8.18	8.50	6.83	6.43
2.11	02/11/20	02/12/16	8.21	8.27	8.65	6.89	6.50
2.12	02/12/23	03/1/30	8.25	8.32	8.72	6.93	6.54
2.13	03/4/17	03/5/15	8.26	8.38	8.85	6.98	6.61
2.14	03/8/4	03/8/26	8.32	8.47	9.00	7.05	6.68
2.15,16	03/11/11	03/12/6	8.35	8.53	9.11	7.09	6.72
2.17	04/2/18	04/3/10	8.34	8.55	9.19	7.11	6.75

(Note) Ver. 2.07 and 2.08 have not been used for level-1 processing.

RCCs depends on the target temperature, any changes in the instrument gain (responsivity) cannot be directly assessed using the radiance difference alone.

One of the purposes of the ASTER vicarious calibration effort is to quantitatively provide an independent assessment of ability of the onboard calibration system to correctly estimate the offset and responsivity (gain) for each of the 50 TIR detectors. In this section, indirect methods are described for analyzing the instrument gain and offsets with the field data.

B. Method for Responsivity Trend Analysis

To analyze an instrument degradation trend, independent of the artifacts introduced by the periodic updating of the RCCs, a responsivity term is introduced (DN per unit radiance).

In (1), the contribution of the C_2 term is a few percent of that of the C_1 term for a typical case, and also the C_2 coefficients have been fixed as mentioned in Section III-A. We therefore simplify the responsivity V for TIR subsystem by

$$V = \frac{1}{C_1}. \tag{8}$$

The C_1 coefficient depends on the temperature of each detector [24], but the detector temperature is normally kept within ± 0.2 K at about 80 K by the cooler [6]. Thus, a change in C_1 will indicate degradation of the instrument, which may be caused by several factors such as lens transmission, mirror reflection, or detector performance or some combination thereof.

The responsivity can be calculated from each of three kinds of C_1: the C_1 applied to an image, the C_1 measured by the LTC, and the C_1 as predicted by VC. Thus, the image-based responsivity is applied to all RCC versions, the LTC-based responsivity is applied to all LTC datasets, and the VC-based responsivity is applied to all VC datasets. The procedure for calculating each responsivity is described below.

TABLE VI
RADIANCE AT 270 K FOR EACH BAND IN WATTS PER SQUARE METER PER STERADIAN PER MICRON

B10	B11	B12	B13	B14
4.915	5.191	5.469	5.876	5.841

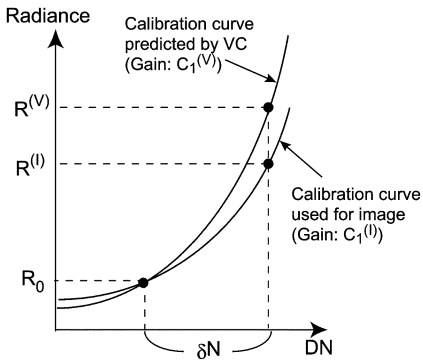

Fig. 8. Relationships among the parameters in (9) giving the VC-based responsivity.

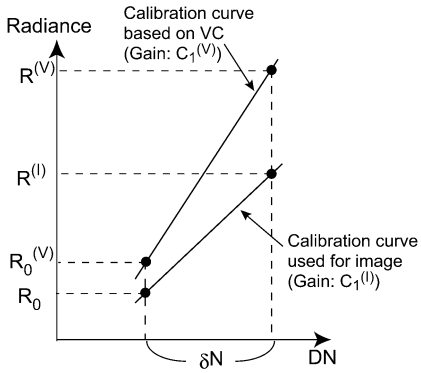

Fig. 9. Relationships among the parameters in (10) giving the VC-based offset at 270 K.

The image-based responsivity $V^{(I)}$ is calculated by $V^{(I)} = 1/C_1^{(I)}$, where $C_1^{(I)}$ is a C_1 applied to the image. Since $C_1^{(I)}$ has been updated in a stepwise manner, $V^{(I)}$ also will change in stepwise manner. Table V shows a list of the RCC version, accompanied with the LTC date (the date of the LTC that each version was measured), the applied date (the first observation date that each version was applied to level-1 processing), and the mean of C_1 over detectors.

The image-based responsivity is not always appropriate for evaluation of instrument degradation, since the C_1 used for calculation does not always have a "true" value at the acquisition time of each image due to stepwise RCC updating. Thus, the LTC-based responsivity $V^{(L)}$ will be more appropriate for such purpose. It is calculated by $V^{(L)} = 1/C_1^{(L)}$, where $C_1^{(L)}$ is a C_1 measured by each LTC.

On the other hand, the C_1 obtained in LTC will not be reliable if the onboard calibrator itself has degraded. The VC-based responsivity should therefore be introduced as a check, and the following method is used for deriving the VC-based responsivity. First, we assume that STC is reliable and each image has no calibration error at 270 K by STC. Under this assumption,

TABLE VII
COEFFICIENTS OF THE REGRESSIVE EQUATION FOR $C_1^{(L)}(D)$ FOR EACH BAND FOR EACH PERIOD [7]. THE COEFFICIENTS FOR THE THIRD PERIOD WERE DERIVED USING ALL DATA

Start day	End day	Coefficient	B10	B11	B12	B13	B14
85	650	a0	7.6940e-3	7.3299e-3	7.1010e-3	6.3132e-3	5.8652e-3
		a1	4.3350e-7	3.7962e-7	4.0530e-7	-1.0811e-6	-1.3399e-6
		a2	-1.2387e-10	1.3728e-9	3.1407e-9	4.3583e-9	5.0933e-9
		a3	3.6673e-13	-9.1356e-13	-2.4717e-12	-3.1286e-12	-3.6291e-12
650	1300	a0	6.0424e-3	5.2127e-3	4.4169e-3	4.2338e-3	3.5926e-3
		a1	5.7039e-6	7.5693e-6	9.8127e-6	6.7513e-6	7.2686e-6
		a2	-5.2967e-9	-6.7810e-9	-8.4413e-9	-6.1424e-9	-6.5348e-9
		a3	1.7348e-12	2.2195e-12	2.7731e-12	2.0135e-12	2.1351e-12
1300	—	a0	7.6679e-3	7.2505e-3	6.9701e-3	6.1247e-3	5.6444e-3
		a1	5.7009e-7	1.0765e-6	1.6884e-6	7.1791e-7	7.5124e-7
		a2	-6.0573e-11	-1.1530e-10	-1.0797e-10	-2.4168e-12	4.4184e-11
		a3	0	0	0	0	0

the VC-based responsivity $V^{(V)}$ can be approximately calculated by

$$V^{(V)} = \frac{1}{C_1^{(V)}} = \frac{1}{C_1^{(I)}} \cdot \frac{R^{(I)} - R_0}{\delta N} \cdot \frac{\delta N}{R^{(V)} - R_0} = V^{(I)} \cdot \frac{R^{(I)} - R_0}{R^{(V)} - R_0} \tag{9}$$

where

$C_1^{(V)}$ C_1 predicted from VC;
$R^{(I)}$ image radiance for a VC site;
$R^{(V)}$ VC-based radiance for the site;
R_0 radiance at 270 K which is constant for each band (Table VI);
δN difference of DN between $R^{(I)}$ and R_0.

The relationships among these parameters are illustrated by Fig. 8. An approximation error caused from nonlinearity is less than 0.5% in responsivity, and the original DN and the RCCs used for the image, which are not contained in ASTER level-1B data (registered radiance at the sensor product) used in our analysis, are not necessary—we can easily apply the equation to level-1B data. In the equation, $R^{(V)}$ and R_0 are perfectly free from a calibration error on the image. $V^{(I)}$ and $R^{(I)}$ are affected by a calibration error caused from delay in RCC updating, but this error will be canceled out to some extent in a product of $V^{(I)}$ and $R^{(I)}$, because the delay in RCC updating will cause overestimation for $V^{(I)}$ and underestimation for $R^{(I)}$. Thus, $V^{(V)}$ may be affected by a calibration error on the image which is included in $V^{(I)}$ and $R^{(I)}$, but it is not significant due to the cancellation. On the other hand, if $R^{(V)}$ is close to R_0, (9) will be unstable. Thus, the equation should be applied to only VC experiment data with target temperature several degrees above or below 270 K.

C. Method for Offset Trend Analysis

In this section, a method for analyzing trends in the offset at 270 K is described which is assumed to be zero in calculation of the VC-based responsivity.

A simple difference between the VC-based radiance and the image-based radiance is a function of the target temperature. Thus, we need to estimate the offset at 270 K. This means that we should estimate the gain (responsivity) and the offset at 270 K simultaneously from a pair of the VC-based radiance and the image-based radiance, but this is an underdetermined problem. Therefore, we first estimate the gain using a regression equation, then estimate the offset. If the target temperature is close to 270 K, an error in the gain estimation will be small. Thus, we used only VCs with low temperatures for the offset trend analysis. A method for this analysis is described below.

When the target temperature is close to 270 K, a linear relationship between two radiances on a calibration curve can be introduced. Thus, using $R = C_1 \delta N + R_0$, the offset at 270 K (δR_0) can be expressed by

$$\delta R_0 = R_0^{(V)} - R_0 = R^{(V)} - R_0 - \frac{C_1^{(V)}}{C_1^{(I)}}(R^{(I)} - R_0) \tag{10}$$

where R_0^V is the VC-based radiance corresponding to DN at R_0. The relationships among these parameters are illustrated by Fig. 9.

Since $C_1^{(V)}$ is unknown, (10) is not solvable. Thus, we substitute $C_1^{(L)}(D)$ for $C_1^{(V)}$, where $C_1^{(L)}(D)$ is a regressive estimate of C_1, and D is the number of days since the launch (December 18, 1999). Hence, the following equation is derived:

$$\delta R_0 = R^{(V)} - R_0 - \frac{C_1^{(L)}(D)}{C_1^{(I)}} \left(R^{(I)} - R_0\right). \tag{11}$$

As for $C_1^{(L)}(D)$, the following cubic function is available [7]:

$$C_1^{(L)}(D) = a_0 + a_1 D + a_2 D^2 + a_3 D^3 \tag{12}$$

where a_0, a_1, a_2, and a_3 are regression coefficients determined for each of three periods divided by a 650-day interval. Table VII shows the coefficients proposed in [7].

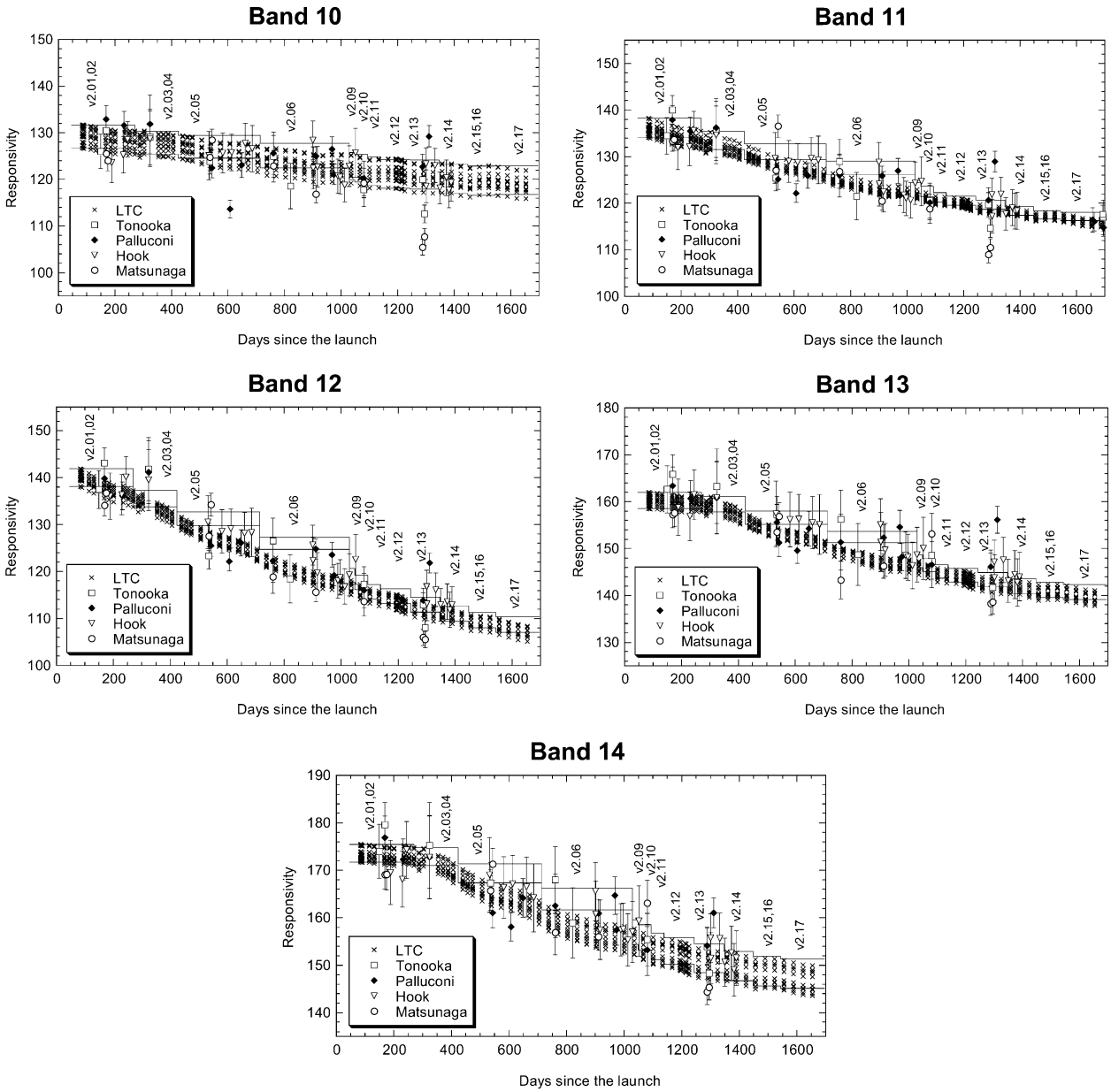

Fig. 10. Responsivity trend plots obtained for bands 10–14. The LTC-based and the VC-based responsivities are shown by points, and the image-based responsivity is shown by the step lines with the RCC versions. The error bar was assumed to be 1% in the at-sensor radiance predicted. The launch date was December 18, 1999.

D. Trend Analysis Results

Using (9) and (11), the responsivity and the offset trends were analyzed. Since the five VC data from CSR were affected by straylight [16], these were excluded and the remaining 74 VC datasets were used for the trend analysis.

As mentioned previously, VC data with high target temperatures will be suitable for the responsivity trend analysis, and those with low target temperatures will be suitable for the offset trend analysis. Thus, 74 VC datasets were separated into two groups with the threshold of 7 °C in the mean at-sensor brightness temperature; 56 VCs with $> 7\,^{\circ}\mathrm{C}$ (shown by C_1 in Table II) were used for the responsivity trend analysis, and 18 VCs with $< 7\,^{\circ}\mathrm{C}$ (shown by C_0 in the table) were used for the offset trend analysis.

1) Responsivity Trend: Fig. 10 shows the responsivity trend plots obtained for bands 10–14. The LTC-based responsivity for each detector, shown by LTC on the plots, was derived from each LTC data by $1/C_1^{(L)}$. Since each band has ten detectors, ten points have been plotted on the same day. As expected, the LTC-based responsivity has been decreasing with time since the launch with each group of detectors (band) showing a common trend [7]. The exact cause behind the degradation is not known, nor why the rate of degradation is band dependent, nor why the rate was discontinuously changed around day 300 (see bands 13 and 14), but the observed trend could be explained by some combination of a decrease in lens transmission, mirror reflection, or detector performance.

The step lines around the LTC-based responsivity points demonstrate the maximum and minimum of the image-based responsivity which were derived by $1/C_1^{(I)}$. The RCC versions are also shown. In the calibration of each ASTER image, the image-based responsivity is assumed to be located between

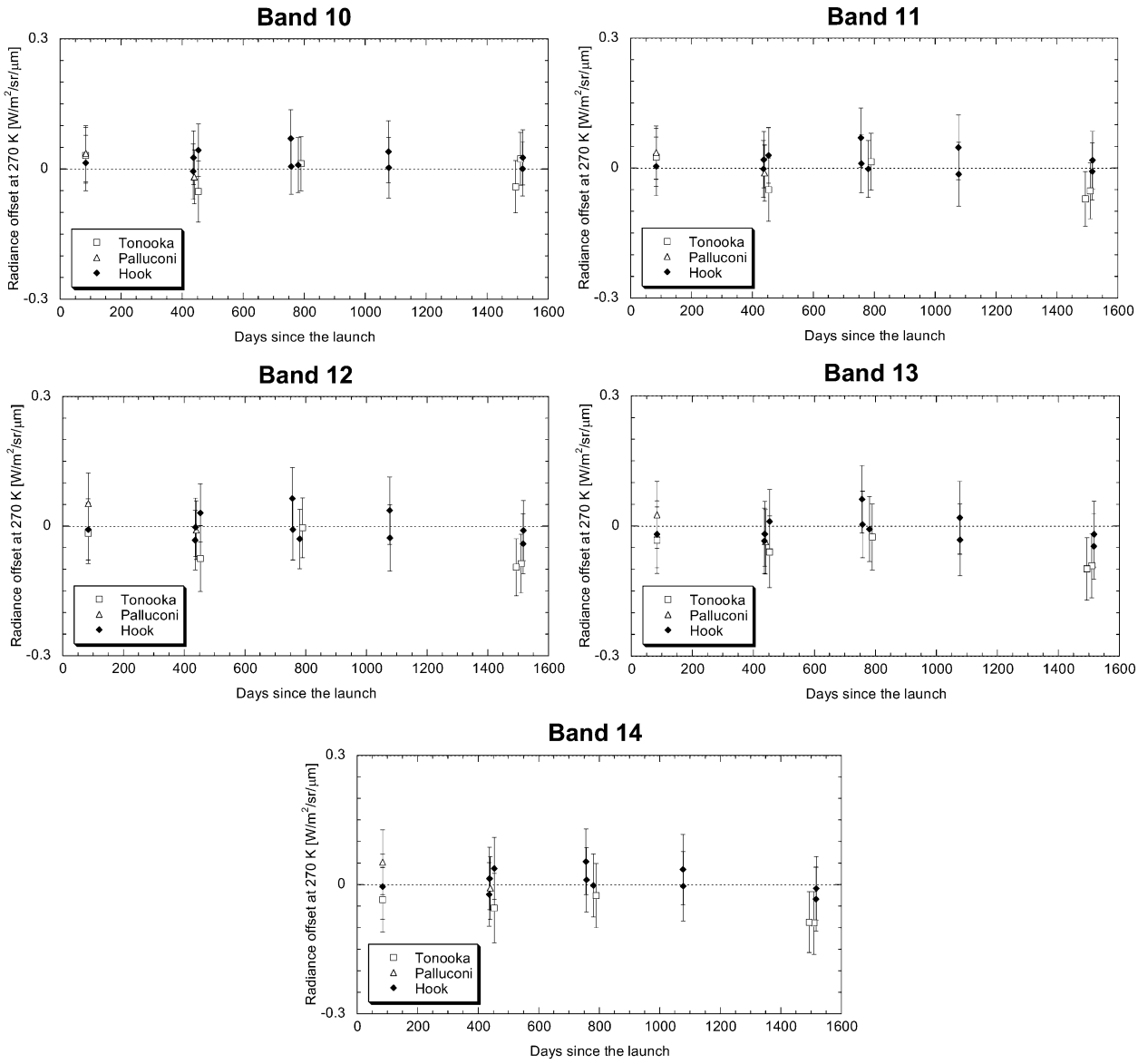

Fig. 11. Trend plots of the offset at 270 K (δR_0), for bands 10–14. The error shown by a bar was assumed to be a combination of 1% in the predicted at-sensor radiance and 1% in $C_1^{(L)}(D)$. The launch date was December 18, 1999.

the maximum and the minimum lines on the image acquisition date. The image-based and the LTC-based responsivities differ in certain periods, particularly for RCC versions 2.05 and 2.06, which indicates that an image radiance will include a calibration error caused from delay in RCC updating.

The other points shown with four investigators' names provide the VC-based responsivity derived by (9). The error shown by a bar was assumed to be 1% in the predicted at-sensor radiance, which is used as an standard for evaluation. The size of 1% will be appropriate for most of water-based VCs, according to sensitivity analysis considering factors such as measured spatial-variation of surface temperature and typical errors of radiosonde profiles (± 1 K for air temperature and $\pm 10\%$ for relative humidity), but may be small for land-based VCs with larger spatial-validations of surface temperature and emissivity.

The LTC-based responsivity estimates are mostly located within the error bars of the VC-based responsivity. The difference between the VC-based and the LTC-based responsivities is less than 10% of the responsivity, on average. Consequently, it can be concluded that the LTC has tracked the responsivity decline observed.

2) Offset Trend: Fig. 11 shows the offset trend plots for bands 10–14 which were obtained from 18 VC data with low target temperatures by (11). The error shown by a bar was assumed to be a combination of 1% in the predicted at-sensor radiance and 1% in $C_1^{(L)}(D)$.

In almost all cases the δR_0 estimates are located well within the vicarious calibration error bars, i.e., the radiance at 270 K predicted from VC $\left(R_0^{(V)}\right)$ agrees with R_0 within the error bar. Therefore, it can be concluded that the STC effectively estimated the radiometric offset of each TIR band.

VIII. Conclusion

Seventy-nine VC experiments were conducted under clear sky conditions in order to assess the radiometric accuracy of the thermal infrared subsystem of the ASTER instrument in-flight. The results indicate that over the first 1400 days average radiance difference over the radiance range 6.5–13 $W/m^2/sr/\mu m$ is 0.5% or better (0.4 K or better in temperature) for all five TIR bands. Fifty-six of the VC datasets were used to assess any changes in instrument gain (responsivity), and 18 of the VC datasets were used to assess any changes in the instrument offset (bias) over time. The results indicate that the long- and short-term calibrations using the onboard calibration system have accurately accounted for the expected change in response (degradation) of the TIR subsystem indicating the OBC has accurately tracked the changing instrument performance.

The results also indicate that the coefficients derived from the onboard calibration data have not always been applied to the instrument data in a sufficiently timely manner to compensate for these changes. At present, there are no plans to reprocess the entire ASTER archive with the appropriate coefficients, and therefore a correction procedure has been developed [7] and is provided via a website [8], that allows any adversely affected scenes, where a delay in the implementation of a calibration update will result in an error in the calibrated instrument data, to be corrected. For the RCC versions 3.00 or later which will be determined by regression equations, this correction will not be necessary.

The ASTER validation team plans to continue to conduct in-flight validation experiments throughout the life of the instrument to ensure the accuracy and integrity of the data provided to investigators using ASTER data thereby ensuring that ASTER data can be used as a long-term climate record where any changes in the calibrated instrument response can be attributed to changes in the climate (including the surface) rather than the instrument.

Acknowledgment

The authors wish to thank the many persons who provided field experiment support, the Earth Remote Sensing Data Analysis Center, Tokyo, for supplying the original ASTER data, and the Japan Resources Observation System Organization, Tokyo, for providing the long-term calibration data. A part of the research described in this paper was carried out at the Jet Propulsion Laboratory, California Institute of Technology, Pasadena.

References

[1] P. Slater, S. F. Biggar, K. Thome, D. I. Gellman, and P. R. Spyak, "Vicarious radiometric calibrations of EOS sensors," *J. Atmos. Oceanic Technol.*, vol. 13, pp. 349–359, 1996.

[2] Y. Yamaguchi, A. B. Kahle, H. Tsu, T. Kawakami, and M. Pniel, "Overview of Advanced Spaceborne Thermal Emission and Reflectance radiometer (ASTER)," *IEEE Trans. Geosci. Remote Sens.*, vol. 36, no. 4, pp. 1062–1071, Jul. 1998.

[3] K. Thome, K. Arai, S. Hook, H. Kieffer, H. Lang, T. Matsunaga, A. Ono, F. Palluconi, H. Sakuma, P. Slater, T. Takashima, H. Tonooka, S. Tsuchida, R. Welch, and E. Zalewski, "ASTER preflight and inflight calibration and the validation of level 2 products," *IEEE Trans. Geosci. Remote Sens.*, vol. 36, no. 4, pp. 1161–1172, Jul. 1998.

[4] H. Fujisada, H. Sakuma, A. Ono, and M. Kudoh, "Design and preflight performance of ASTER instrument protoflight model," *IEEE Trans. Geosci. Remote Sens.*, vol. 36, no. 4, pp. 1152–1160, Jul. 1998.

[5] A. Ono, F. Sakuma, K. Arai, Y. Yamaguchi, H. Fujisada, P. Slater, K. Thome, F. Palluconi, and H. Kieffer, "Preflight and in-flight calibration plan for ASTER," *J. Atmos. Oceanic Technol.*, vol. 13, pp. 321–335, 1996.

[6] H. Fujisada, "ASTER level-1 data processing algorithm," *IEEE Trans. Geosci. Remote Sens.*, vol. 36, no. 4, pp. 1101–1112, Jul. 1998.

[7] H. Tonooka, F. Sakuma, M. Kudoh, and K. Iwafune, "ASTER/TIR onboard calibration status and user-based recalibration," *Proc. SPIE*, vol. 5234, pp. 191–201, 2003.

[8] H. Tonooka. (2003) ASTER TIR Level-1B Recalibration. Earth Remote Sensing Data Analysis Center (ERSDAC), Tokyo. [Online]. Available: http://www.science.aster.ersdac.or.jp/RECAL/index.html.

[9] A. Berk, L. S. Bernstein, and D. C. Robertson, "MODTRAN: A moderate resolution model for LOWTRAN-7," Geophysics Lab., Hanscom AFB, MA, GLTR-89-0122, 1989.

[10] S. J. Hook. (1999) The ASTER Spectral Library. Jet Propulsion Lab., California Inst. Technol., Pasadena, CA. [Online]. Available: http://speclib.jpl.nasa.gov.

[11] Z. Wan, Y. Zhang, X. Ma, M. D. King, J. S. Myers, and X. Li, "Vicarious calibration of the Moderate Resolution Imaging Spectroradiometer airborne simulator thermal-infrared channels," *Appl. Opt.*, vol. 38, pp. 6294–6306, 1999.

[12] J. W. Salisbury and D. M. D'Aria, "Emissivity of terrestrial materials in the 8–14 μm atmospheric window," *Remote Sens. Environ.*, vol. 42, pp. 83–106, 1992.

[13] I. J. Barton, P. J. Minnett, K. A. Maillet, C. J. Donlon, S. J. Hook, A. T. Jessup, and T. J. Nightingale, "The Miami2001 infrared radiometer calibration and intercomparison: 2. Ship board results," *J. Atmos. Oceanic Technol.*, vol. 21, pp. 268–283, 2004.

[14] C. J. Bruegge, N. L. Chrien, R. R. Ando, D. J. Diner, W. A. Abdou, M. C. Helmlinger, S. H. Pilorz, and K. J. Thome, "Early validation of the Multi-angle Imaging Spectroradiometer (MISR) radiometric scale," *IEEE Trans. Geosci. Remote Sens.*, vol. 40, no. 7, pp. 1477–1492, Jul. 2002.

[15] K. J. Thome, S. F. Biggar, and W. Wisniewski, "Cross comparison of EO-1 sensors and other earth resources sensors to Landsat-7 ETM+ using Railroad Valley Playa," *IEEE Trans. Geosci. Remote Sens.*, vol. 41, no. 6, pp. 1180–1188, Jun. 2003.

[16] H. Tonooka, "Inflight straylight analysis for ASTER thermal infrared bands," *IEEE Trans. Geosci. Remote Sens.*, vol. 43, no. 12, pp. 2752–2762, Dec. 2005.

[17] H. Tonooka, F. Palluconi, T. Matsunaga, M. Shoji, and K. Arai, "Early results from the vicarious calibration activities for ASTER/TIR in Japan," *J. Remote Sens. Soc. Jpn.*, vol. 21, pp. 440–448, 2001.

[18] F. D. Palluconi, H. Tonooka, A. Abtahi, R. E. Alley, T. Thompson, G. Hoover, and S. Zadourian, "EOS ASTER midinfrared band vicarious calibration," *Proc. SPIE*, vol. 4540, pp. 255–259, 2002.

[19] J. P. Rice, J. J. Butler, B. C. Johnson, P. J. Minnett, K. A. Maillet, T. J. Nightingale, S. J. Hook, A. Abtahi, C. J. Donlon, and I. J. Barton, "The Miami2001 infrared radiometer calibration and intercomparison: 1. Laboratory characterization of blackbody targets," *J. Atmos. Oceanic Technol.*, vol. 21, pp. 258–267, 2004.

[20] E. Kalnay, M. Kanamitsu, and W. E. Baker, "Global numerical weather prediction at the National Meteorological Center," *Bull. Amer. Meteorol. Soc.*, vol. 71, pp. 1410–1428, 1990.

[21] S. J. Hook, A. J. Prata, R. E. Alley, A. Abtahi, R. C. Richards, S. G. Schladow, and S. Ó Pálmarsson, "Retrieval of lake bulk-and skin-temperatures using Along Track Scanning Radiometer (ATSR) data: A case study using Lake Tahoe, CA," *J. Atmos. Oceanic Technol.*, vol. 20, no. 2, pp. 534–548, 2003.

[22] S. J. Hook, G. Chander, J. A. Barsi, R. E. Alley, A. Abtahi, F. D. Palluconi, B. L. Markham, R. C. Richards, S. G. Schladow, and D. L. Helder, "In-flight validation and recovery of water surface temperature with Landsat-5 thermal infrared data using an automated high-altitude lake validation site at Lake Tahoe CA/NV, USA," *IEEE Trans. Geosci. Remote Sens.*, vol. 42, no. 12, pp. 2767–2776, Dec. 2004.

[23] S. J. Hook and A. B. Kahle, "The micro Fourier transform interferometer (μFTIR)—A new field spectrometer for validation of infrared data," *Remote Sens. Environ.*, vol. 56, pp. 172–181, 1996.

[24] ASTER Science Team, "Algorithm Theoretical Basis Document for ASTER Level-1 Data Processing, Ver. 3.0, ERSDAC LEL/8-9," Earth Remote Sensing Data Analysis Center, Level-1 Data WG, Tokyo, Japan, 1996.

Hideyuki Tonooka (M'04) received the B.Eng., M.Eng., and D.Eng. degrees from the University of Tokyo, Tokyo, Japan, in 1992, 1994, and 2000, respectively.

Since 1994, he has been a member of the faculty of Ibaraki University, Ibaraki, Japan. His current post at the university is Associate Professor in the Center for Information Technology. He is a member of the Project Science Team for the Advanced Spaceborne Thermal Emission and Reflection radiometer (ASTER), part of the National Aeronautics and Space Administration's Earth Observing System, and he is also a member of the Thermal Infrared Science Team for the Greenhouse gas Observing SATellite (GOSAT) under development by the Japan Aerospace Exploration Agency and the Ministry of the Environment of Japan. His main research activities are in thermal infrared remote sensing and data fusion techniques.

Frank D. Palluconi is a Member of the Jet Propulsion Laboratory, Pasadena, CA, and has an interest in thermal measurement instrumentation, atmospheric correction, and their application to the understanding of planetary surfaces and surface processes. He is a NASA Earth Observing System ASTER Team Member, a Landsat-7 Calibration Team Member, and a Scientist working on the Mars Science Laboratory 2009 Rover Mission.

Simon J. Hook received the B.Sc. degree from the University of Durham, Durham, U.K., the M.Sc. degree from the University of Alberta, Edmonton, AB, Canada, and the Ph.D. degree from the University of Durham, in 1982, 1985, and 1989, respectively, all in geology.

From 1989 to 1991, he was a National Research Council Resident Research Associate with the National Aeronautics and Space Administration Jet Propulsion Laboratory (JPL), Pasadena, CA. Since 1991, he has been a Technical Staff Member at JPL. From 1993 to 2003, he was the Project Scientist for the Advanced Spaceborne Thermal Emission and Reflectance Radiometer (ASTER). In addition to his work on ASTER, he has been involved in the validation of several airborne and spaceborne instruments, including Landsat-5 and ETM+, the Moderate Resolution Imaging Spectroradiometer (MODIS), MASTER (the MODIS/ASTER Airborne Simulator), the European Along-Track Scanning Radiometers (ATSR2 and AATSR), and the DOE Multispectral Thermal Imager. His research is focused on the use of solar reflective and thermal infrared remotely sensed data in geology and ecology with a special emphasis on in-flight calibration and validation.

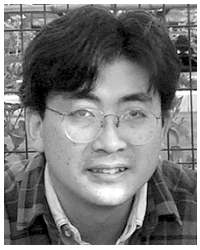

Tsuneo Matsunaga received the B.S., M.S., and Ph.D. degrees on engineering from the University of Tokyo, Tokyo, Japan, in 1990, 1992, and 1997, respectively.

He joined the Geological Survey of Japan in 1992, and then the Tokyo Institute of Technology in 1998. He has been a Senior Researcher at the National Institute for Environmental Studies, Tsukuba, Japan, since 2001 and an Adjunct Professor, University of Tsukuba since 2005. His current research interests are instrument and algorithm development for environmental and geologic remote sensing. He is a Member of the Japan/U.S. joint ASTER Science Team and a Principal Investigator of the Spectral Profiler instrument onboard JAXA's SELENE lunar exploring spacecraft.

Dr. Matsunaga is a member of several academic societies including the Remote Sensing Society of Japan, the International Society of Optical Engineering, and the American Geophysical Union.